



# Bandgap engineering of NiWO<sub>4</sub>/CdS solid Z-scheme system via an ion-exchange reaction

Mingjie Li, Shun Yokoyama, Hideyuki Takahashi\*, Kazuyuki Tohji

Graduated School of Environmental Studies, Tohoku University, Sendai, 982–8579, Japan

## ARTICLE INFO

### Keywords:

Z-scheme system  
Bandgap engineering  
NiWO<sub>4</sub>/CdS  
Hydrogen generation

## ABSTRACT

Energy band alignment is essential for efficient charge transfer and solar light utilization in the solid Z-scheme system (SZSS). Here, we propose a strategy to fabricate the NiWO<sub>4</sub>/CdS composition as SZSS with an additional feature of a tunable bandgap via an ion-exchange reaction between the NiWO<sub>4</sub> precursor and Cd<sup>2+</sup>/S<sup>2-</sup>, which is confirmed with SEM-EDS and Raman spectroscopy. UV–vis DRS and photoluminescence spectrometry determine the bandgap structures. Photosystem II is constructed from NiWO<sub>4</sub>, while the structure of photosystem I (PSI) depends on the S content in the composition. As the S content increases from 0 to 45 at%, the bandgap decreases from 2.62 to 1.86 eV for PSI. Moreover, the photoluminescence spectra and photocatalytic H<sub>2</sub> generation experiments demonstrate that the introduction of S provides the proper band alignment for efficient charge transfer and H<sub>2</sub> generation. Bandgap engineering in SZSS by adjusting the S content in the NiWO<sub>4</sub>/CdS composition can be also extended to other metal tungstate and metal sulfide composites (MWO<sub>4</sub>/MS).

## 1. Introduction

The conversion of solar light into clean H<sub>2</sub> through a photocatalytic process is an attractive solution to the problems associated with carbon energy. However, directly splitting water via a photocatalyst in a single component creates a conflict between the large energy band potential demanded for water splitting ( $\Delta G = 237.2$  kJ/mol,  $\Delta E = 1.23$  V) and the narrow bandgap required to efficiently utilize visible light [1]. Multiple component systems such as type II and pn heterojunction (Scheme 1a) effectively enhance the charge transfer efficiency via a combination of different materials [2], but the efficiency increases at the expense of the energy band potential, which is undesirable for water splitting.

Another multiple component system that has attracted much attention since being discovered in 2006 is the solid Z-scheme system (SZSS) [3]. This system imitates natural photosynthesis. SZSS (Scheme 1b) can generate electrons and holes using visible light without decreasing the redox potential, which is essential for photocatalytic H<sub>2</sub> generation [4]. SZSS is fabricated by two functionalized parts, which are called photosystem I (Psi) and photosystem II (PSII).

Psi and PSII are used in the reduction and oxidation reaction, respectively. The interface between Psi and PSII is specially designed as an ohmic contact to facilitate the migration of electrons from the conduction band (CB) of PSII to the valence band (VB) of Psi. Because CB in

Psi has a higher potential than that in PSII, while VB in PSII has a lower potential than that in Psi. Electrons and holes in CB of Psi and VB of PSII respectively with higher redox abilities can join in the redox reaction.

Some important factors determine the efficiency of SZSS: (1) the physicochemical properties of materials used as Psi and PSII; (2) interface between Psi and PSII and (3) the energy band alignment of Psi and PSII. During the last few years, many studies have investigated the interface properties such as the exploration of different materials like metals [5,6], carbon dots [7], and oxygen-defect [8] as electron mediators to facilitate the charge transfer between Psi and PSII. However, a rational design of the band alignment of Psi and PSII has yet to be discovered. Considering the conflict between the large energy demand for water splitting and the requirement for visible light utilization, controlling the energy bandgap in SZSS is essential.

Element modulation is an important way to control light absorption and engineer the bandgap for multiple component materials. Introducing foreign elements to form an impurity energy level can create a bandgap change in semiconductors. Additionally, changing the element composition in the alloyed structures has successfully engineered the bandgap in solid solutions such as Zn<sub>x</sub>Cd<sub>1-x</sub>Se [9] and Zn<sub>x</sub>Cd<sub>1-x</sub>S [10]. Recently, metal tungstates such as NiWO<sub>4</sub>, CoWO<sub>4</sub>, CuWO<sub>4</sub>, and ZnWO<sub>4</sub> have been developed as promising photocatalysts to decompose contaminants [11,12]. Highly efficient photocatalytic H<sub>2</sub> generation has been reported using the CdWO<sub>4</sub>/CdS structure as a type

\* Corresponding author.

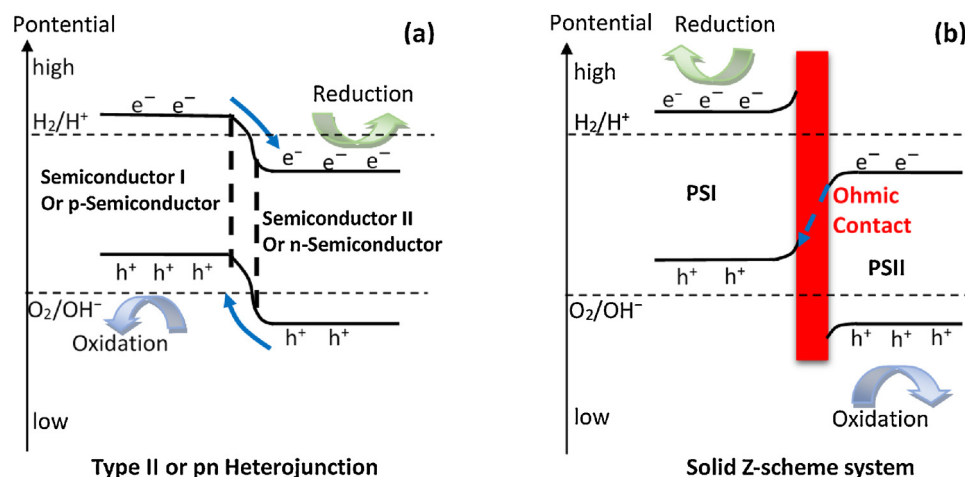
E-mail address: [hideyuki.takahashi.c2@tohoku.ac.jp](mailto:hideyuki.takahashi.c2@tohoku.ac.jp) (H. Takahashi).

<https://doi.org/10.1016/j.apcatb.2018.09.050>

Received 30 May 2018; Received in revised form 11 September 2018; Accepted 16 September 2018

Available online 17 September 2018

0926-3373/ © 2018 Elsevier B.V. All rights reserved.



Scheme 1. Type II or pn heterojunction (a) and SZSS (b).

II heterojunction [13,14] or SZSS [8]. However, element modulation and bandgap engineering have yet to be achieved. The special ion-exchange reaction between the  $NiWO_4$  precursor and ions of  $Cd^{2+}$ ,  $S^{2-}$  reported herein provides a novel method for element modulation and bandgap engineering.

In this research,  $NiWO_4/CdS$  SZSS is fabricated under mild reaction conditions using ion-exchange between the  $NiWO_4$  precursor and  $Cd^{2+}$ ,  $S^{2-}$  ions. This novel method easily realizes element modulation by changing the stoichiometry of the reactants in a synthetic solution. The effect of the element composition on the energy band, charge transfer mechanism, and photocatalytic activity in  $H_2$  generation are reported. These results should provide interesting information for the rational design and fabrication of SZSS in the future.

## 2. Experimental

### 2.1. Materials

$Ni(NO_3)_2 \cdot 6H_2O$  (98%),  $Na_2WO_4 \cdot 2H_2O$  (99–100.5%),  $Cd(CH_3COO)_2 \cdot 2H_2O$  (99.9%),  $CH_3CSNH_2$  (98%),  $H_2PtCl_6 \cdot 6H_2O$  (98.5%),  $NaBH_4$  (95.0%), lactic acid (85.0–92.0%) were used as received from Wako Chemical.

### 2.2. Fabrication of SZSS

Scheme S1 in the supplementary information shows the synthetic procedure and the formation mechanism of the samples, respectively.  $NiWO_4$  was synthesized by the ion precipitation method. While stirring, 5 mL of 0.6 mol/L  $Ni(NO_3)_2 \cdot 6H_2O$  solution and  $Na_2WO_4 \cdot 2H_2O$  solution were added simultaneously into 60 mL water. After a 1.5-h reaction time, the precipitate was filtered and dried in a vacuum overnight, yielding  $NiWO_4$ .

Next Pt was modified on  $NiWO_4$ .  $NiWO_4$  (0.5 g) and 0.5 mL of 0.02 g/mL  $H_2PtCl_6 \cdot 6H_2O$  solution ( $Pt/NiWO_4 = 1.18$  at%) were mixed in 97.5 mL water. Then a  $NaBH_4$ /ethanol solution (0.02 g in 2 mL) was added dropwise and the suspension was stirred for 15 min. Then sample was filtered and dried in a vacuum overnight and labeled as NW.

NW was used as a precursor to fabricate SZSS by an ion reaction with  $Cd^{2+}$  and  $S^{2-}$  in solution. NW (0.21 g) was dispersed in water so the total volume was 70 mL, 2.1 mL of 0.02 g/mL  $Cd(CH_3COO)_2 \cdot 2H_2O$  (the  $Cd^{2+}$  resource), and certain amounts of 0.005 g/mL  $CH_3CSNH_2$  (the  $S^{2-}$  resource) were added to the suspension while stirring. Then the suspension was heated at 80 °C for 2 h. The amounts of  $CH_3CSNH_2$  solution added in this step were 0, 2.8, 8.4, and 14 mL, and the corresponding products were labeled as NWCS0, NWCS15, NWCS30, and NWCS45, respectively, based on the S content (at%) within four kinds

of elements (Ni, W, Cd and S) measured by SEM-EDS. Finally, the sample was filtered and dried in a vacuum overnight. As a comparison, NWS30 was synthesized from a reaction between NW and  $CH_3CSNH_2$  solution (14 mL) without using  $Cd^{2+}$ . NWCS45 (Pt 2.36 at%) and NWCS45 (Pt 4.72 at%) were synthesized from NW precursors with Pt content of  $Pt/NiWO_4 = 2.36$  and 4.72 at% respectively.

### 2.3. Photocatalytic activities (PCA) in $H_2$ generation

The photocatalyst (0.05 g) and about 130 mL 1:10 V:V lactic acid/water solution were placed in the photocatalytic reactor. After sonicating for 5 min, the suspension was irradiated by a Xenon lamp (550 W KXL-552HPF, Wacom) and the volume of generated gas was measured. The irradiation area was  $4\pi \text{ cm}^2$ , and the light intensity at 420 nm was  $4.9 \text{ mW/cm}^2$ . After the reaction, 10  $\mu\text{L}$  of gas was removed from the reactor via a syringe and measured by gas chromatography (GC-3200, GL Sciences) equipped with a molsieve 5 A column and a TCD detector.

### 2.4. Characterization

Scanning electron microscopy (SEM, SU-8000, Hitachi) and transmission electron microscopy (TEM, EM-002B, Topcon) evaluated the morphology of the samples. The elemental composition was examined by the energy dispersive X-ray spectrometer attached to SEM (SEM-EDS), and the data was obtained as the average of five different zones. The crystal state was analyzed by X-ray diffractometry (XRD, multiflex, Cu K $\alpha$  source, Rigaku) in  $0.02^\circ$  steps. Structural information was collected by Raman spectrometry (NRS-5100, JASCO) using a 532-nm laser and a resolution of  $4.2 \text{ cm}^{-1}$  ( $0.67 \text{ cm}^{-1}/\text{pixel}$ ). The data was obtained as the average of three different zones. Light absorption was evaluated by UV-vis diffuse reflectance spectrometry (UV-vis DRS, U-3300 Hitachi), while photoluminescence (PL) spectrometry (F-7000 High Tech, Hitachi) at a 200-nm excitation wavelength and at a photo-voltage of 700 V was used to assess the charge transfer properties. The data was obtained as the average of three measurements.

## 3. Results and discussion

### 3.1. Structure and morphology

Fig. 1 shows the XRD patterns of NW and NWCS30. The wide halo peak from  $20$  to  $40^\circ$  in the NW pattern may be due to amorphous  $NiWO_4$ . However, a low crystalline state cannot be excluded because the main peak of crystal state  $NiWO_4$  (00-015-0755) is also located within this region. After NW reacting with  $Cd^{2+}$  and  $S^{2-}$  at 80 °C (Fig. 1, NWCS30), several signals appear around  $27.2^\circ$ ,  $35.6^\circ$ ,  $50.9^\circ$  and  $53.8^\circ$ .

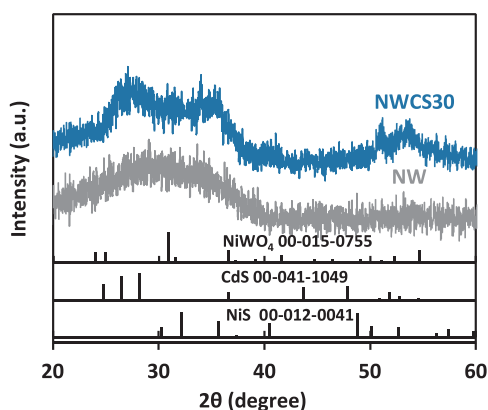


Fig. 1. XRD patterns of NW and NWS30.

The generation of peaks compared with NW pattern indicate that the cation and the anions in NWS30 do not construct a simple uniform amorphous state. As the binding force between  $\text{Ni}^{2+}$ ,  $\text{Cd}^{2+}$  cations, and  $\text{WO}_4^{2-}$ ,  $\text{S}^{2-}$  anions differ, various compositions may be generated in the crystalline state. However, the peak positions do not match those of bulk crystalline  $\text{NiWO}_4$ ,  $\text{CdS}$  and  $\text{NiS}$  perfectly. The low signal/noise ratio may be one of the reasons for the mismatch. Another may be the complex interrelationship of  $\text{Ni}^{2+}$ ,  $\text{Cd}^{2+}$  cations and  $\text{WO}_4^{2-}$ ,  $\text{S}^{2-}$  anions in the multiphase, leading to a change in the crystal structure.

The inner structures of the materials were further analyzed from the Raman spectra (Fig. 2). NW shows an intense peak at  $881.2\text{ cm}^{-1}$  and several weak peaks at approximately  $691$ ,  $540$ ,  $415$ ,  $357$ ,  $210$ , and  $145\text{ cm}^{-1}$ . These agree with the Raman features of the  $\text{NiWO}_4$  crystal reported by Elizabeth et al. [15]. Additionally, the broad peak centered at  $950\text{ cm}^{-1}$  is assigned to the main peak of amorphous  $\text{NiWO}_4$  [16]. This broad peak disappears gradually in the patterns of NWS0–NWS45, suggesting that some of the amorphous phase is transferred to the crystal phase or other compounds without Raman signals during the synthetic reaction. The characteristic peaks of NWS0–NWS45 are almost consistent with those of NW, but the peaks associated with  $\text{CdS}$  and  $\text{NiS}$  are not observed. This may be because the Raman signals of  $\text{CdS}$ / $\text{NiS}$  in the amorphous state are too low to be observed or covered by the  $\text{NiWO}_4$  signals.

The Raman spectra also reveal that the intense peak shifts in the region of  $880.0\text{--}888.7\text{ cm}^{-1}$  (Fig. 2b). The intense peak is due to the W–O bond vibration of the  $\text{WO}_6$  unit in  $\text{NiWO}_4$  with a wolframite structure [15]. Compared with NW, the peak center of the NWS0 spectrum shifts dramatically from  $881.2$  to  $888.7\text{ cm}^{-1}$ , which is towards the characteristic peak of  $\text{CdWO}_4$  ( $895\text{ cm}^{-1}$ ) [17]. This shift is attributed to the distortion of the  $\text{WO}_6$  unit due to the introduction of  $\text{Cd}^{2+}$  and the formation of  $\text{CdWO}_4$  in the  $\text{NiWO}_4$  structure. This phenomenon provides evidence of the interaction between  $\text{Cd}^{2+}$  and the  $\text{WO}_6$  unit in the multiphase.

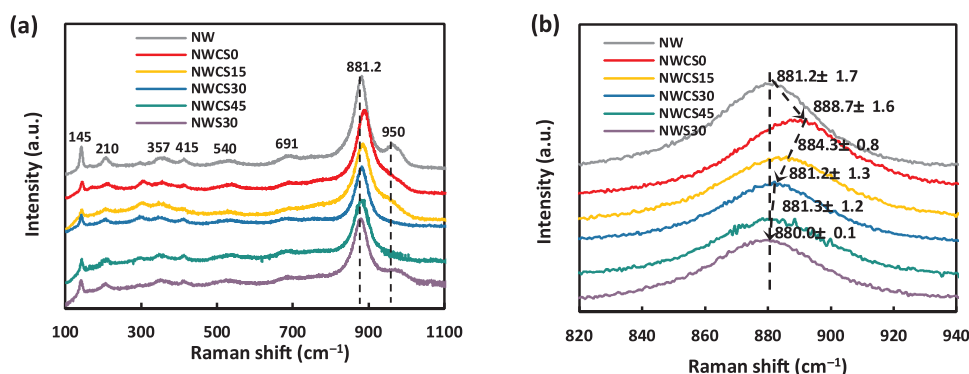


Fig. 2. Raman spectra (a) and details for the intense peaks (b) of the samples.

On the other hand, the intense peak of NWS30 appears at approximately  $880.0\text{ cm}^{-1}$ . This is close to that of NW, demonstrating that introducing S does not distort  $\text{WO}_6$ . After introducing 15 at% S in NWS15, the peak center is reduced to  $884.3\text{ cm}^{-1}$ . Further increasing the S content reduces the peak center position until it reaches  $881.2$  and  $881.3\text{ cm}^{-1}$  in NWS30 and NWS45, respectively. The distortion of  $\text{WO}_6$  induced by  $\text{Cd}^{2+}$  disappears as S increases, suggesting that  $\text{Cd}^{2+}$  tends to combine with  $\text{S}^{2-}$  to produce  $\text{CdS}$  in these samples. Therefore, this “back-shift” provides evidence of the combination of  $\text{S}^{2-}$  and  $\text{Cd}^{2+}$  in the multiphase.

Fig. 3 shows the morphology of the samples from SEM and TEM. NW are spherical particles with 100–200-nm diameters (Fig. 3a). The TEM image of NW (Fig. 3f) shows that the spherical particles have defined edges with circular shapes, indicating that the particles may be aggregates of many smaller particles. NWS0 particles are a few microns in size (Fig. 3b), while NWS30 particles range from hundreds of nanometers to a few microns (Fig. 3c). These observations indicate that the reaction with  $\text{Cd}^{2+}$  is the primary cause of aggregation. SEM confirms that NWS30 is comprised of irregularly shaped particles from 100 nm to a few microns (Fig. 3d). TEM demonstrates that the edges become indistinct and irregular (Fig. 3g), which sharply contrasts those from NW. This irregular structure should be produced from the reaction between  $\text{NiWO}_4$  and ions of  $\text{Cd}^{2+}$ / $\text{S}^{2-}$ . The SEM image in Fig. S1 shows that the morphology of NWS15 and NWS45 are similar with that of NWS30.

SEM-EDS mapping of NWS30 demonstrates that Ni, W, Cd, and S are distributed uniformly on the particle (Fig. 3e). Pt cannot be observed because its concentration is too low ( $\text{Pt}/\text{NiWO}_4 = 1.18\text{ at\%}$  in the synthetic solution of NW). This result indicates that reaction between the  $\text{NiWO}_4$  precursor and the ions of  $\text{Cd}^{2+}$ ,  $\text{S}^{2-}$  leads to the formation of tiny and uniformly distributed Cd and S related components on the  $\text{NiWO}_4$  particle surface.

### 3.2. Ion-exchange reaction

To reveal the composition of the samples, Fig. 4 and Table 1 show the proportion of Ni, Cd, W, and S measured by SEM-EDS. NW was synthesized from the precipitation reaction between  $\text{Ni}^{2+}$  and  $\text{WO}_4^{2-}$  ions (Eq. (1)). The EDS result shows that the ratio of Ni to Cd is close to 1:1, supporting the  $\text{NiWO}_4$  structure. Compared with NW, part of W is “replaced” by S in NWS30, implying an anion-exchange reaction between  $\text{S}^{2-}$  and  $\text{WO}_4^{2-}$  may occur during the synthesis of NWS30 (Eq. (2)). The solubility product constants ( $k_{\text{sp}}$ ) of  $\text{NiWO}_4$  and  $\text{NiS}$  theoretically support this ion-exchange reaction. Because  $k_{\text{sp}}\text{NiS}$  ( $1.4 \times 10^{-24}$ ) [18] is much lower than  $k_{\text{sp}}\text{NiWO}_4$  ( $7.8 \times 10^{-6}$ ) [19],  $\text{NiS}$  is more stable than  $\text{NiWO}_4$  under the same conditions. Consequently,  $\text{NiS}$  is easily generated in a solution of  $\text{NiWO}_4$  and  $\text{S}^{2-}$  because the ions tend to form a stable compound. Similarly, the part of Ni replaced by Cd in NWS0 may be induced from the cation-exchange reaction between  $\text{Cd}^{2+}$  and  $\text{NiWO}_4$  (Eq. (3)).



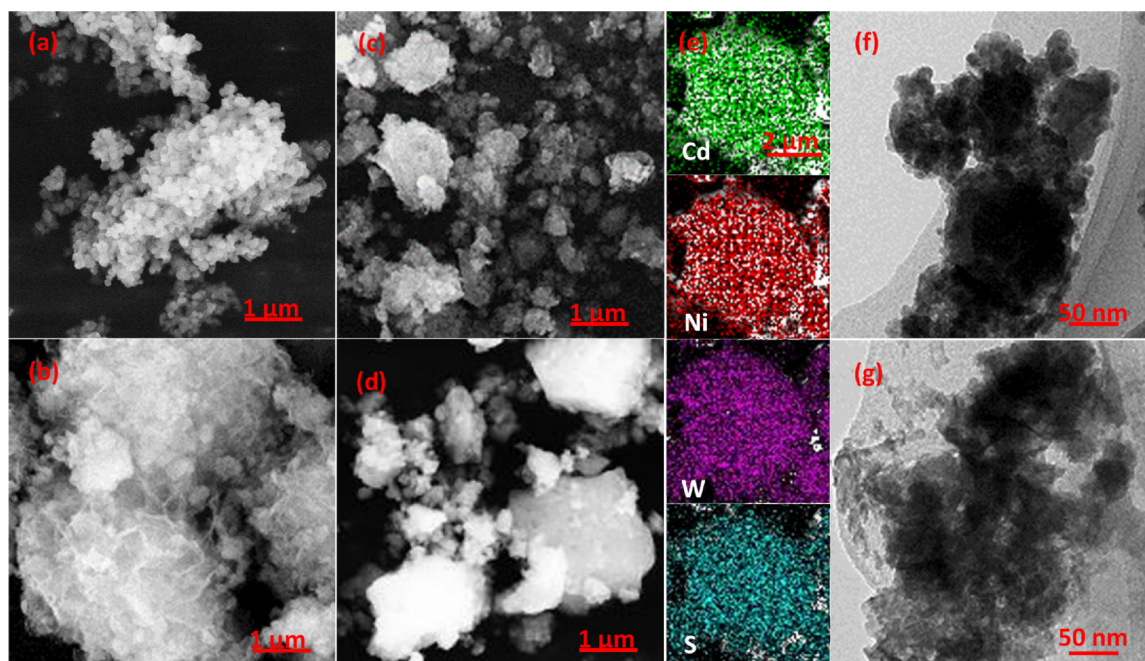


Fig. 3. SEM images of NW (a), NWCS0 (b), NWS30 (c), NWCS30 (d), EDS–MAPPING (e); and TEM images of NW (f), NWCS30 (g).

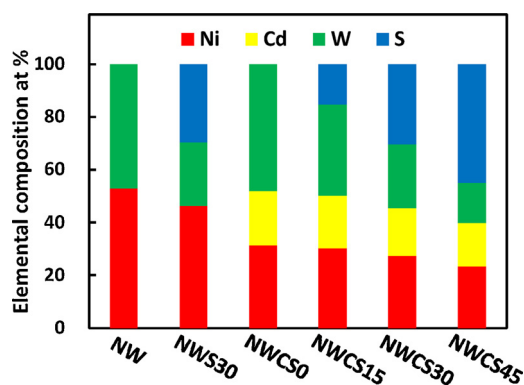
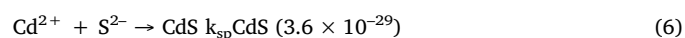
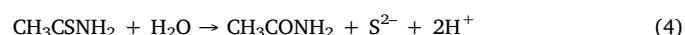
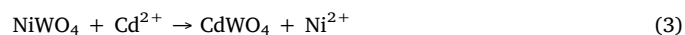
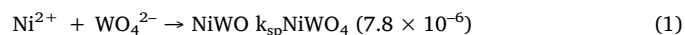


Fig. 4. Proportion of Ni, Cd, W and S in samples measured by SEM–EDS.

In NWCS15, NWCS30, and NWCS45, the proportion of Ni and Cd remains nearly constant, while S increases and W decreases dramatically as  $\text{CH}_3\text{CSNH}_2$  increases in a synthetic solution. The reactions during the synthesis of NWCS15–30 can be described as follows. First,  $\text{CH}_3\text{CSNH}_2$  releases  $\text{S}^{2-}$  continuously and slowly in an 80 °C solution through a hydrolysis reaction (Eq. (4)). When the concentration of  $\text{S}^{2-}$  is low,  $\text{CdWO}_4$  is initially produced via a cation-exchange reaction (Eq. (3)), but as  $\text{S}^{2-}$  increases,  $\text{CdS}$  ( $k_{\text{sp}} = 3.6 \times 10^{-29}$ ) [18] can be produced from the anion-exchange reaction between  $\text{CdWO}_4$  and  $\text{S}^{2-}$  (Eq. (5)) or the precipitation reaction (Eq. (6)). When an excess  $\text{S}^{2-}$  exists in solution compared with  $\text{Cd}^{2+}$ , an anion-exchange reaction may occur, and

$\text{NiS}$  is generated (Eq. (2)). Accordingly, the anion-exchange reaction between  $\text{WO}_4^{2-}$  and  $\text{S}^{2-}$  (Eqs. (2) and (5)) is responsible for the decrease of W in the samples of NWCS15–45. The interaction of  $\text{Cd}^{2+}$  and  $\text{WO}_6$  or  $\text{S}^{2-}$  shown in the Raman spectra before the reaction supports the cation/anion-exchange reaction (Eqs. (2),(3), and 5) proposed here.

This ion-exchange reaction provides a simple way for element modulation under mild conditions.



### 3.3. Light absorption and energy bandgap

Fig. 5 shows the UV–vis absorbance spectra of the samples. NW displays a strong peak with maximum around 242 nm, which is related to the charge transfer transition in  $\text{NiWO}_4$  [15]. Therefore, the absorption edge corresponding to 242 nm is assigned to the energy bandgap of  $\text{NiWO}_4$  ( $E_{\text{g1}}$ ). The spectra of NWCS0–NWCS45 exhibit the new absorption edges at higher wavelengths ( $E_{\text{g2}}$ ), which are discontinuous with  $E_{\text{g1}}$ . The discontinuous absorption edges indicate that the multiphase has a heterogeneous composition, which is consistent

Table 1

Elemental composition, bandgap structure, PL intensity and PCA (H2) of the samples.

Samples	Elements at%				PSI E <sub>g</sub> 2			PL 10 <sup>3</sup> a.u.	PCA mL/h		
	Ni	Cd	W	S	CdWO <sub>4</sub>	CdS(CdWO <sub>4</sub> ) <sub>x</sub>	CdS(NiS) <sub>x</sub>				
NW	53.0	0.0	47.0	0.0	2.62 eV	2.53 eV	2.02 eV	3.32	0.3		
NWCS0	31.3	20.6	48.2	0.0				2.74			
NWCS15	30.2	20.1	34.5	15.3				1.57			
NWCS30	27.4	18.1	24.3	30.3				0.38	7.3		
NWCS45	23.6	16.3	15.2	45.0				1.86 eV	0.42	7.0	

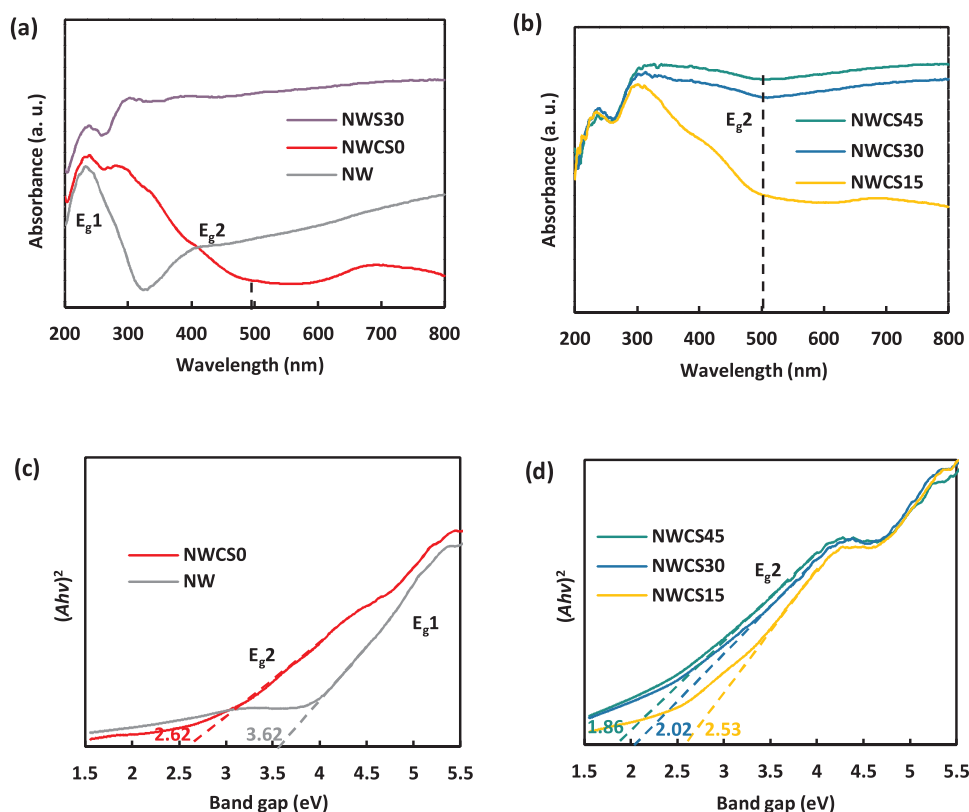


Fig. 5. UV-vis absorbance spectrum (a, b) and corresponding  $(Ah\nu)^2-h\nu$  curves (c, d) of samples.

with abovementioned results. Therefore, the absorption edge at  $E_{g2}$  may be induced in other semiconductors with different energy bands. Sethi et al. also reported two discontinuous absorption edges induced from bandgap of  $\text{CdWO}_4$  and CdS in the  $\text{CdWO}_4/\text{CdS}$  composition [14]. Additionally, NWCS15–45 show strong absorption in the region of 400–800 nm compared with NW. This visible light absorption may be induced by NiS, because NWS30 also shows the similar absorption in the same region.

$$ah\nu = C(h\nu - E_g)^{n/2} \quad (7)$$

The bandgaps can be calculated by Eq. (7), where  $E_g$ ,  $\alpha$ ,  $h\nu$ , and  $C$  are the band gap, absorption coefficient, photon energy and a constant, respectively. The “ $\alpha$ ” was replaced by the “ $A$ ” (absorbance) in this research [20]. “ $n$ ” is determined by the direct ( $n = 1$ ) or indirect ( $n = 4$ ) absorption type of the semiconductors. NiS and CdS are widely regarded as direct semiconductors [21,22], whereas both direct and indirect bandgaps of  $\text{NiWO}_4$  [12,23] and  $\text{CdWO}_4$  [8,24] have been reported. Fig. 5c, d and Fig. S2 show the curves for  $(Ah\nu)^2-h\nu$  and  $(Ah\nu)^{0.5}-h\nu$ , respectively. Based on the property of the curves,  $n = 1$  was used in this research, and the bandgap was obtained from the intercepts of  $(Ah\nu)^2-h\nu$  curves.

Fig. 6a displays the corresponding bandgap value. In NWCS0–45, as the S content increases from 0 to 45 at%, the bandgap decreases from 2.62 to 1.86 eV for  $E_{g2}$ .  $E_{g1}$  of NWCS0–45 should be constructed by  $\text{NiWO}_4$ , which are represented by the  $\text{NiWO}_4$  bandgap in NW (3.62 eV, close to the literature 2.95 eV [12]; 4.5 eV [15]).  $E_{g2}$  of NWCS0 should be constructed by  $\text{CdWO}_4$  because the Raman spectra confirms the presence of  $\text{CdWO}_4$  in this sample. The low bandgap value of  $\text{CdWO}_4$  in our research compared with bulk  $\text{CdWO}_4$  (3.74 eV) [8] may be because here  $\text{CdWO}_4$  is formed by the cation-exchange reaction. The co-hybridization of both Ni and Cd with  $\text{O}_{2p}$  and  $\text{W}_{5d}$  may induce band bending of  $\text{CdWO}_4$ .  $E_{g2}$  of NWCS15 is 2.53 eV, which is located between  $\text{CdWO}_4$  (2.62 eV) and bulk CdS (2.4 eV) [25]. In contrast, the  $E_{g2}$  values are 2.02 and 1.86 eV for NWCS30 and NWCS45, respectively.

These values agree well with the  $(\text{NiS})_x(\text{CdS})_{(1-x)}$  multicomponent (1.65–2.2 eV) [21] rather than bulk CdS (2.4 eV) or NiS (0.4 eV) [25]. Therefore,  $E_{g2}$  of NWCS15–45 should be mainly constructed by CdS but is influenced by the doping compounds such as  $\text{CdWO}_4$  for NWCS0 and NiS for NWCS30–45. The doping compounds create an impurity energy level that leads to a change in the bandgap of CdS.

Table 1 summarizes the band structures based on the results of the ion-exchange reaction and the bandgap information. Based on the energy bandgap theory, introducing a foreign element can induce bandgap bending in a semiconductor by changing the crystal structure and the electron distribution due to the volume and electronegativity difference of the induced element, respectively [26]. As shown in Table 2, the ionic radius and electronegativity of Cd and S drastically differ from those of Ni, W, and O. Therefore, it is easy to understand why the ion-exchange reaction can induce bandgap bending. The decrease of bandgap is attributed to the change of the inner structure or the electron distribution induced by the foreign  $\text{Cd}^{2+}$  and  $\text{S}^{2-}$  ions with different ionic radii and electronegativities.

The PL spectra also support the proposed bandgap structure (Fig. 6b). NW displays a broad emission peak in the region from 330 to 420 nm with a maximum at approximately 363 nm. This maximum is related to the bandgap of NW (3.62 eV corresponding to 342 nm), suggesting that the emission peak is induced by a charge recombination within the energy band of  $\text{NiWO}_4$  [27]. For NWCS0, the peak maximum is slightly redshifted to 380 nm, indicating that the ion-exchange reaction with  $\text{Cd}^{2+}$  (Eq. (3)) induces the bandgap bending of  $\text{NiWO}_4$ . Compared with NW, a new emission band (420–550 nm) related to  $\text{CdWO}_4$  [28] appears, providing evidence for the formation of a  $\text{CdWO}_4$  energy band in NWCS0. Introducing S in NWCS15–NWCS30 decreases the emission band to a flat shape without forming the characteristic peaks of CdS or NiS. The consistency of data from both UV-vis DRS and PL spectra supports the bandgap structure proposed before.

Fig. 7 shows the PL intensity at approximately 380 nm and the PCA in  $\text{H}_2$  generation as a function of S content. Corresponding gas ( $\text{H}_2$ )

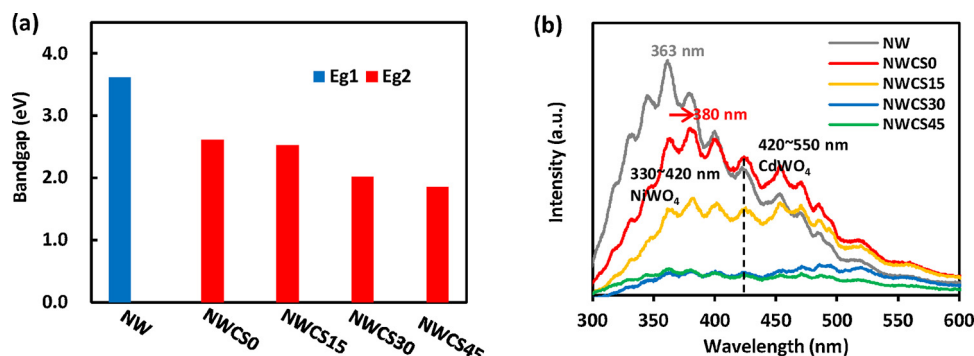


Fig. 6. Bandgap value (a), and PL spectrum (b) of the samples.

Table 2

Ionic radius and electronegativity of the elements.

Elements	Ionic radius (nm)	Electronegativity
Ni	0.069 ( $\text{Ni}^{2+}$ )	4.40
Cd	0.095 ( $\text{Cd}^{2+}$ )	4.33
W	0.06 ( $\text{W}^{6+}$ )	4.40
O	0.14 ( $\text{O}^{2-}$ )	7.54
S	0.184 ( $\text{S}^{2-}$ )	6.22

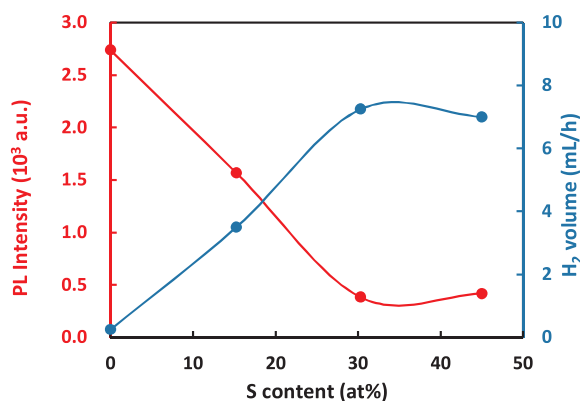


Fig. 7. PL intensity at approximately 380 nm and photocatalytic  $\text{H}_2$  generation rates as a function of S content in samples.

generation curves were shown in Figure S3a. The PL intensity decreases dramatically as the S content increases from 0 to 30 at%, but then slightly increases at 45 at%. On the other hand, PCA increases sharply as the S content increases from 0 to 30 at%, but then slightly decreases

at 45 at%. The PL intensity at approximately 380 nm provides an index of the charge recombination rate in  $\text{E}_{\text{g}1}$ . The increased charge separation rate and PCA should be related to the change in the band structure induced by the S content in the multicomponent system.

Figure S3b shows the effect of Pt content on PCA. When the Pt content increases from 1.18 at% to 2.36 at%, the PCA increases from 7.0 to 7.8 mL/h (the average of 2-h reaction). Further increases the Pt content to 4.72 at% only slightly increases the PCA to 7.9 mL/h. These results reveal that a spot of Pt can benefit the charge transfer within SZSS.

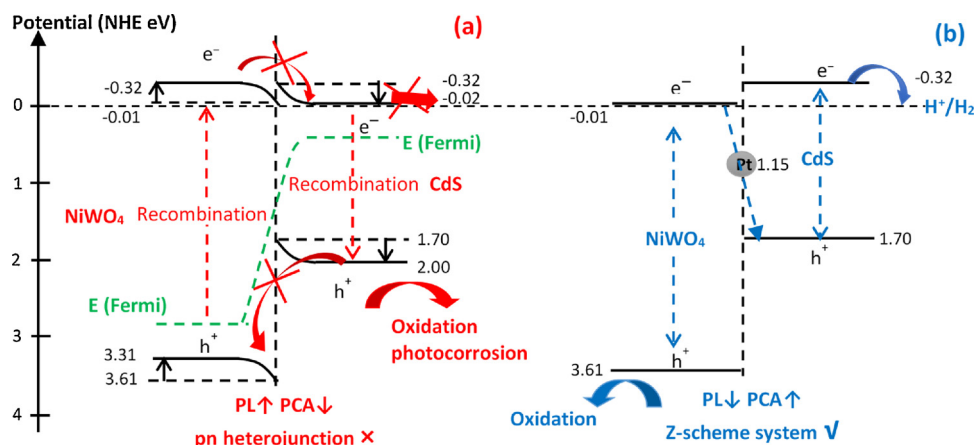
### 3.4. Charge transfer mechanism and bandgap engineering

To reveal the charge transfer mechanism in this multicomponent system, the conduction band potential ( $E_{\text{VB}}$ ) and valence band potential ( $E_{\text{CB}}$ ), which are related to the normal hydrogen electrode (NHE) of  $\text{E}_{\text{g}1}$  and  $\text{E}_{\text{g}2}$ , were calculated from Eqs. (8) and (9) [29].  $\chi$  is the electronegativity of the semiconductor and is determined by the geometric average of the atoms.  $E_{\text{e}}$ , which is the free electron energy vs. NHE, is 4.5 eV. VB and CB of  $\text{E}_{\text{g}2}$  are calculated based on the main component inducing the bandgap, which is  $\text{CdWO}_4$  for NWCS0 and  $\text{CdS}$  for NWCS15–NWCS45. Schemes 2 and 3 show the calculated results.

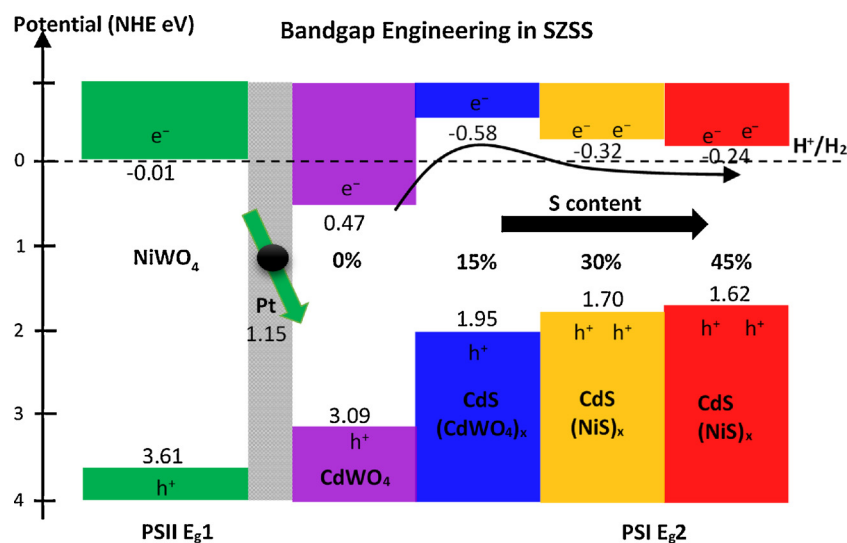
$$E_{\text{CB}} = \chi - E_{\text{e}} - 0.5 E_{\text{g}} \quad (8)$$

$$E_{\text{VB}} = E_{\text{CB}} + E_{\text{g}} \quad (9)$$

There are two kinds of charge transfer paths of NWCS30. Scheme 2a is the traditional “pn-type” path between p-type  $\text{NiWO}_4$  [30,31] and n-type  $\text{CdS}$ . The internal electric field formed at the interface can result in energy band bending (usually 0.3–0.4 eV) for both semiconductors. However, as  $E_{\text{CB}}$  and  $E_{\text{VB}}$  of  $\text{CdS}$  are much higher than those of  $\text{NiWO}_4$ , band bending can lead to energy barriers at the interface, prohibiting



Scheme 2. Charge transfer mechanism in pn heterojunction (a) or SZSS (b) of NWCS30.



Scheme 3. Bandgap alignments in SZSS as a function of S content.

electron and hole migration. Obviously, this band alignment is unfavorable for charge separation and  $H_2$  generation, which is inconsistent with the experiment results shown in Fig. 7.

Actually, the pn heterojunction can be formed only when the interface between two semiconductors is in a high purity state without defects. In this experiment, a spot of Pt (work function is 1.15 eV vs NHE) was modified on  $NiWO_4$  by  $NaBH_4$ , which may create a conductive layer as the ohmic contact at the interface. As a consequence, band alignment of NWCS30 can be constructed as SZSS in Scheme 2b. The electrons in the CB of  $NiWO_4$  can migrate across the conductive layer and recombine directly with holes in VB. The “Z-type” charge migration can decrease the carrier recombination rate in both  $NiWO_4$  and CdS, creating holes and electrons with a higher redox ability. This charge transfer model is in consist with the results shown in Fig. 7. The formation of CdS through the introduction of S provides the proper band alignment for the “Z-type” charge migration and  $H_2$  generation. Hence, the PL intensity decreases while PCA in  $H_2$  generation increases as the S content increases from 0 to 45 at%. The PL and PCA results shown in Fig. 7 indicate that the charge transfer mechanism is primarily in “Z-type” path. However, the unfavorable “pn-type” path cannot be excluded from the SZSS.

Scheme 3 shows the bandgap alignments of NWCS0–NWCS45 SZSS. The bandgap of pure  $NiWO_4$  is too large for visible light absorption. Although the cation-exchange reaction with  $Cd^{2+}$  produces  $CdWO_4$  as PSI with a narrow bandgap,  $E_{CB}$  is not favorable for  $H_2$  generation. The introduction of S with a low electronegativity via an anion-exchange reaction produce CdS with higher  $E_{CB}$  for the  $H_2$  generation reaction. Further increasing the S content decreases CdS bandgap by introducing an impurity energy level. This decreased bandgap enables the utilization of a light source with a longer wavelength for PSI, which is essential for the photocatalytic activity of SZSS. On the other hand,  $E_{CB}$  of CdS also decreases as the S content increases, limiting the  $H_2$  generation in the SZSS. This decrease of  $E_{CB}$  in CdS may be the reason for the decrease in the  $H_2$  generation rate from NWCS30 to NWCS45. In summary, element modulation of the S content via ion-exchange reaction provides a simple method to engineer the bandgap for PSI in  $NiWO_4$ /CdS SZSS.

Fig. 8 shows the stability of NWCS45 (Pt 2.36 at%). Photocatalytic reaction rates are from 6.2 to 8.8 mmol/h/g in the first 6-h reaction, then decrease to 4.7 mmol/h/g in 6–8-h reaction. The decrease may be attributed to the photocorrosion of CdS in lactic acid solution [8]. Many researchers reported that SZSS can increase the stability of metal sulfide [8,32]. Because in “Z-type” charge transfer path, oxidation reaction place is changed from VB of metal sulfide to VB of PSII (usually

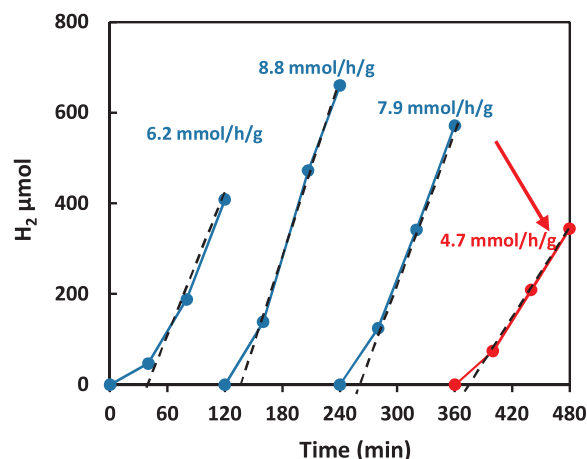


Fig. 8.  $H_2$  generation curves and stability of NWCS45 (Pt 2.36 at%). Before every round of 2nd–4th, about 110 mL after-reaction solution was replaced by fresh lactic acid solution. The reaction rates were evaluated by the 40–120 min reaction in every round.

constructed by stable metal oxide materials), which can prevent metal sulfide from photocorrosion. However, in this work,  $NiWO_4$ /CdS SZSS seems not so stable towards photocorrosion in lactic acid solution. As shown in Scheme 2, the unfavorable “pn-type” charge transfer path which cannot be excluded may be the reason for relative low stability: in “pn-type” path, holes in CdS cannot transfer to  $NiWO_4$  efficiently, the accumulated holes in CdS VB may induce the photocorrosion.

$H_2$  generation rate of NWCS45 (Pt 2.36 at%) was evaluated by the average of 1–3 rounds. As shown in Table S1, the rate reaches 7.6 mmol/h/g, which is higher than many reported SZSS and traditional CdS, demonstrating the high performance of  $NiWO_4$ /CdS. As discussed above, “Z-type” charge transfer path is the key factor for both PCA and stability of SZSS. Therefore, the research point in our next step is to increase “Z-type” charge transfer efficiency through a balance of charge transfer between PSII and PSI, in order to increase the PCA and stability of  $NiWO_4$ /CdS.

#### 4. Conclusion

Rational design of the band alignment in SZSS is essential to develop practical applications. In the traditional method, SZSS is usually fabricated via the synthesis of PSI (or PSII) on PSII (or PSI) as a supporter.



Although the weight ratio of PSII/Psi can be changed, the band alignment cannot be adjusted. Using the NiWO<sub>4</sub>/CdS composition as a representative, we developed a novel fabrication method that takes advantage of bandgap engineering through a simple ion-exchange reaction between the NiWO<sub>4</sub> precursor and Cd<sup>2+</sup>, S<sup>2-</sup>. The bandgaps of PSI decrease from 2.62 to 1.86 eV. Furthermore, this bandgap engineering method could be extended to fabricate SZSS using other metal tungstates and metal sulfides (MWO<sub>4</sub>/MS) in order to obtain SZSS with a high efficiency.

## Acknowledgement

This work was supported by JSPS KAKENHI Grant Number 17K18967.

## Appendix A. Supplementary data

Supplementary material related to this article can be found, in the online version, at doi:<https://doi.org/10.1016/j.apcatb.2018.09.050>.

## References

- [1] D.L. Lu, T.Y. Takata, N.B. Saito, et al., *Nature* 440 (2006) 295.
- [2] S.J.A. Moniz, S.A. Shevlin, D.J. Martin, et al., *Energy Environ. Sci.* 8 (2015) 731–795.
- [3] H. Tada, T. Mitsui, T. Kiyonaga, et al., *Nat. Mater.* 5 (2006) 782–786.
- [4] P. Zhou, J.G. Yu, M. Jaroniec, *Adv. Mater.* 26 (2014) 4920–4935.
- [5] W.B. Li, C. Feng, S.Y. Dai, et al., *Appl. Catal. B* 168–169 (2015) 465–471.
- [6] X.W. Wang, G. Liu, L.Z. Wang, et al., *Adv. Energy Mater.* 2 (2012) 42–46.
- [7] X.Q. Wu, J. Zhao, L.P. Wang, et al., *Appl. Catal. B* 206 (2017) 501–509.
- [8] X. Jia, M. Tahir, L. Pan, et al., *Appl. Catal. B* 198 (2016) 154–161.
- [9] J. Xu, X. Yang, H.K. Wang, et al., *Nano Lett.* 11 (2011) 4138–4143.
- [10] Q. Li, H. Meng, P. Zhou, et al., *ACS Catal.* 3 (2013) 882–889.
- [11] U.M. García-Pérez, A.M.–D.L. Cruz, J. Peral, *Electrochim. Acta* 81 (2012) 227–232.
- [12] T. Montini, V. Gombac, A. Hameed, et al., *Chem. Phys. Lett.* 498 (2010) 113–119.
- [13] L. Wang, W.Z. Wang, *Cryst. Eng. Commun.* 14 (2012) 3315–3320.
- [14] Y.A. Sethi, R.P. Panmand, S.R. Kadam, et al., *J. Colloid Interfaces Sci.* 487 (2017) 504–512.
- [15] E.I.R. Medgaarden, I.E. Wachs, *J. Phys. Chem. C* 111 (2007) 15089–15099.
- [16] A. Kuzmin, J. Purans, R. Kalendarev, *Ferroelectrics* 258 (2001) 21–30.
- [17] J.J. Xu, M.D. Chen, Z.M. Wang, *Dalton Trans.* 43 (2014) 3537–3544.
- [18] Weast, R.C. *Handbook of Chemistry and Physics*. 1982–1983. p. B-242.
- [19] D.L. Zeng, W.W. Yi, *J. Cent. South Inst. Min. Metall.* 25 (1994) 6.
- [20] H.G. Yu, J.G. Yu, B. Cheng, et al., *J. Solid State Chem.* 179 (2006) 349–354.
- [21] A.U. Ubale, A.N. Bargal, *Mater. Res. Bull.* 46 (2011) 1000–1010.
- [22] W. Chen, G.R. Duan, T.Y. Liu, et al., *J. Mater. Sci.* 50 (2015) 3920–3928.
- [23] P.K. Pandey, N.S. Bhavne, R.B. Kharat, *Electrochim. Acta* 51 (2006) 4659–4664.
- [24] J.R. Fuertes, A. Fredrich, D. Errandonea, et al., *Phys. Rev. B* 95 (2017) 174105.
- [25] Y. Xu, M.A.A. Schoonen, *Am. Mineral* 85 (2000) 543–556.
- [26] S.H. Wei, S.B. Zhang, A. Zunger, *J. Appl. Phys.* 87 (2000) 1304–1311.
- [27] S.M. Pourmortazavi, M.R. Nasrabadi, M.K. Shalamzari, et al., *Appl. Surf. Sci.* 263 (2012) 745–752.
- [28] M. Hojamberdiev, R. Kanakala, O. Ruzimuradov, et al., *Opt. Mater. (Amst)* 34 (2012) 1954–1957.
- [29] K.N. Ding, B. Chen, Z.X. Fang, et al., *Theor. Chem. Acc.* 132 (2013) 1352.
- [30] T.H. Kim, C.H. Kwak, J.H. Lee, *ACS Appl. Mater. Interfaces* 9 (2017) 32034–32043.
- [31] M. Pirhashemi, A.H. Yangjeh, *Sep. Purif. Technol.* 193 (2018) 69–80.
- [32] K. Iwashina, A. Iwase, Y.H. Ng, et al., *J. Am. Chem. Soc.* 137 (2015) 604–607.